INTERFACE

rsif.royalsocietypublishing.org

The atypically high modulus of pollen exine

Zihao Qu and J. Carson Meredith

School of Chemical and Biomolecular Engineering, Georgia Institute of Technology, Atlanta, GA, USA

JCM, 0000-0003-2519-5003

Research

Cite this article: Qu Z, Meredith JC. 2018 The atypically high modulus of pollen exine. *J. R. Soc. Interface* **15**: 20180533. http://dx.doi.org/10.1098/rsif.2018.0533

Received: 14 July 2018
Accepted: 17 August 2018

Subject Category:
Life Sciences–Physics interface

Subject Areas:
biomaterials, biomechanics, biophysics

Keywords:
pollen exine, sporopollenin, elastic modulus, nanoindentation, mechanical property mapping

Author for correspondence:
J. Carson Meredith
e-mail: carson.meredith@chbe.gatech.edu

Electronic supplementary material is available online at http://dx.doi.org/10.6084/m9.figshare.c.4209887.

THE ROYAL SOCIETY PUBLISHING

Sporopollenin, the polymer comprising the exine (outer solid shell) of pollen, is recognized as one of the most chemically and mechanically stable naturally occurring organic substances. The elastic modulus of sporopollenin is of great importance to understanding the adhesion, transport and protective functions of pollen grains. In addition, this fundamental mechanical property is of significant interest in using pollen exine as a material for drug delivery, reinforcing fillers, sensors and adhesives. Yet, the literature reports of the elastic modulus of sporopollenin are very limited. We provide the first report of the elastic modulus of sporopollenin from direct indentation of pollen particles of three plant species: ragweed (*Ambrosia artemisiifolia*), pecan (*Carya illinoinensis*) and Kentucky bluegrass (*Poa pratensis*). The modulus was determined with atomic force microscopy by using direct nanomechanical mapping of the pollen shell surface. The moduli were atypically high for non-crystalline organic biomaterials, with average values of 16 ± 2.5 GPa (ragweed), 9.5 ± 2.3 GPa (pecan) and 16 ± 4.0 GPa (Kentucky bluegrass). The amorphous pollen exine has a modulus exceeding known non-crystalline biomaterials, such as lignin (6.7 GPa) and actin (1.8 GPa). In addition to native pollen, we have investigated the effects of exposure to a common preparative base–acid chemical treatment and elevated humidity on the modulus. Base–acid treatment reduced the ragweed modulus by up to 58% and water vapour exposure at 90% relative humidity reduced the modulus by 54% (pecan) and 72% (Kentucky bluegrass). These results are in agreement with recently published estimates of the modulus of base–acid-treated ragweed pollen of 8 GPa from fitting to mechanical properties of ragweed pollen–epoxy composites.

1. Introduction

Plant pollens are among the most unique naturally occurring microparticles. Pollen grains are microscopic capsules carrying male gametes for plant reproduction. They have evolved optimized exine shells with remarkable structure and surface chemistry to facilitate pollination and germination. Recently, pollen grains have attracted increasing research interest due to their unique adhesion characteristics, low weight, high mechanical strength, functionalizability, fluorescence and biocompatibility [1]. For example, Fadiran & Meredith used vinyltrimethoxysilane-functionalized ragweed pollen to reinforce poly(vinyl acetate). The resulted polymer–pollen composite showed an 80% increase in tensile strength and a wider glass transition [2]. Similarly, ragweed pollen were recently reported to result in a 47% increase in tensile strength, a 70% increase in strain at break and a 14% increase in modulus of epoxy composites at 10 wt% pollen loading [3]. Uddin *et al*. [4,5] have demonstrated the oral delivery of vaccines to mice via ragweed pollen and the potential for pollen to be used for controlled release of pharmaceuticals has been reviewed [6]. Moreover, pollen have been used as templates for fabricating metal-oxide magnetic replicas [7,8], magnetic-core particles [9] and metallized shells [10] with unique combinations of multimodal adhesion and optical properties.

A native pollen shell consists of three domains from outside to inside: (i) pollenkitt, (ii) exine and (iii) intine [11]. The pollenkitt is an adhesive and viscous liquid coated on the exine. It can protect pollen from drying, promote adhesion and support pollination. The exine is the tough outer solid wall that often bears spines, bumps or grooves and exhibits an enormous species-specific diversity of morphology due to the size and shape of these surface features. The intine, made of cellulose, is a thin wall just inside the exine surrounding the generative cells inside the pollen shell. The exine influences adhesion and determines the external surface chemistry and mechanical properties of pollen grains. The exine is mainly composed of sporopollenin, one of the most chemically and thermally stable biological polymers [12,13]. The chemical composition of sporopollenin has been a subject of study and debate [14], but the most recent consensus suggests that it consists of saturated and unsaturated aliphatic chains with conjugated aromatics that are highly cross-linked by ester or ether bonds to form a rigid structure. Meanwhile, the surface of the pollen exine contains hydroxyl groups that provide facile sites for functionalization [15]. The mechanical properties of sporopollenin are rarely reported in the literature, but they are of great importance to the natural protective performance and adhesion behaviour of pollen shells. For example, it was shown recently that the spines on sunflower and ragweed pollen particles can lock onto similarly sized features on flower stigma surfaces, resulting in pressure-dependent adhesion behaviour [16]. High modulus could support this unusual particle adhesive function, because of the frictional forces that would arise when pollen grains are pressed onto stigma hair features. In addition, some researchers reported that the mechanical properties of pollen shells were of great importance to understanding the contaminant adhesion on gecko skin [17]. The pollen modulus and its dependence on relative humidity (RH) are also expected to be important in the process of harmomegathy, in which desiccating pollen grains fold inwardly and lessen water loss by blocking pollen apertures [18]. This dehydration-induced folding and its reversal upon rehydration at the stigma are dependent on the modulus, and yet the dependence of sporopollenin modulus on water vapour exposure is unknown. Two somewhat-indirect measurements of the modulus of pollen shells have been reported. Liu *et al*. used a micromanipulation technique to measure the product of Young's modulus and the wall thickness ($E \times h$) of desiccated ragweed pollen to be $1653 \pm 36\ \mathrm{N\ m^{-1}}$ under compression [19]. To obtain this value from compression data, a model of the pollen shell was required, and the pollen grain was treated as a smooth, spherical capsule with an air-filled core and an impermeable wall. Because the pollen shell is actually a porous wall with elaborate surface morphology, a technique that does not require a morphological model would be desirable. Another paper used two-phase composite models to extract the ragweed pollen modulus of 8 GPa from mechanical measurements of epoxy–pollen composites [3]. However, this approach depends on assumptions of the model, which neglects particle surface morphology and imperfections in the adhesive interface between pollen and polymer. Because these prior estimates of the modulus are relatively high for an organic, non-crystalline material, a direct measurement is preferable for confirming whether these prior estimates are reasonable.

Atomic force microscopy (AFM) measures the force on a cantilever tip as a function of its vertical position. The resulting 'force–distance (f–d) curves' can be analysed to determine properties of the material beneath the tip, including adhesion, topography and stiffness [20]. However, these f–d curves can only provide data at one point on the material at a time. The technique of force volume imaging can collect f–d curves from a large number of pixels to create a map of the properties across the sample [21]. Nevertheless, it is typically too slow to map properties over a large sample. To solve this problem, the so-called pulsed force mode was developed in 1997 [22]. This technique improves speed by using a relatively fast sinusoidal ramping of the probe. Unfortunately, this also makes measurements of material properties less quantitative [22,23]. Peak force tapping, developed in 2010, reduces mapping time from hours (force volume mode) to minutes (peak force tapping) for a 5 μm × 5 μm area [23]. Meanwhile, it also allows one to measure the complete f–d curve on each pixel, and precisely control peak force applied to the substrate. This technology enabled a technique known as peak force quantitative nanomechanical property mapping (PFQNM), with which mechanical properties can be mapped as a topological image containing stiffness, adhesion and topography information with nanoscale resolution [23,24]. By carefully selecting the AFM probe, one can measure elastic moduli from 1 MPa to 100 GPa without destroying the sample. PFQNM mode has been demonstrated to be an effective technique for characterizing both soft and hard materials in the literature, such as living cells [25], diatoms [26], polymer composites [27], cement [28] and steel [29].

In this paper, PFQNM AFM was used as a direct method to measure, for the first time, the elastic moduli of three types of pollen shells (ragweed, pecan and Kentucky bluegrass). These three types of pollen shells represent a broad variety including common flowering weeds, trees and grasses, covering a range of morphologies from echinate (spines are longer than 1 μm in length) to spinulose (spines are less than 1 μm in length). Meanwhile, the elastic moduli of pollen shells could be influenced by common chemical treatments and water vapour exposure, important for commercial applications or in the natural environment. Therefore, the ragweed pollen was treated with an acid followed by a base washing, commonly used for cleaning pollen, to investigate the effect of the treatment on the elastic modulus. Furthermore, the pecan and Kentucky bluegrass moduli were measured after exposure to a 90% RH environment, to understand the effect of water saturation on the elastic modulus.

2. Experimental section

2.1. Materials

The native non-defatted pollen grains of three different species were purchased from Greer Laboratories (Lenoir, NC, USA) and stored at 0°C, including ragweed (*Ambrosia artemisiifolia*), pecan (*Carya illinoinensis*) and Kentucky bluegrass (*Poa pratensis*). Methanol, ethanol and chloroform were purchased from Sigma–Aldrich and used as received. Two types of silicon AFM probes, RTESPA-300 and RTESPA-525, were purchased from Bruker. A set of standard samples (PFQNM-SMPKIT-12M) was obtained from Bruker to calibrate the probes and AFM system. Silicon wafers were purchased from University-Wafer, Inc. (South Boston, MA, USA). Epoxy glues (LOCTITE®, 2 h setting time) were purchased from Henkel Corporation (Rocky Hill, CT, USA) to fix pollen gains on the silicon

wafer. Potassium hydroxide (KOH, EMD Millipore) and phosphoric acid (H_3PO_4, BDH Chemicals) were used for base–acid treatment.

2.2. Sample preparation

Prior to use, the pollen grains were washed with a mixture of chloroform and methanol (3 : 1), which is a good solvent for the pollenkitt coating on the pollen grains [1]. The washed pollen grains were rinsed with ethanol and dried at ambient conditions (20°C and 24% RH) for 24 h. The resulting pollen grains are referred to as the cleaned pollen of ragweed (CPr), pecan (CPp) and Kentucky bluegrass (CPk). CPr was further treated with KOH and H_3PO_4 by methods described in detail elsewhere [2]. The resulting ragweed pollen was referred to as base–acid-treated ragweed pollen (BAPr) and used to investigate the effect of AB treatment on Young's modulus of ragweed pollen. In addition, exposure to elevated humidity was studied. CPp and CPk were stored in 90% RH for 24 h to prepare water-saturated pollen (WSPp and WSPk). WSPp and WSPk were re-saturated in the 90% RH environment every 30 min for 10 min during AFM measurements. To avoid the movement of the pollen grains during the AFM measurements, pollen grains were glued onto a Piranha-cleaned Si wafer with a thin layer of epoxy resin by using a micromanipulator (NARISHIGE, Japan) and an optical microscope (Olympus BX51) [30].

2.3. Scanning electron microscopy

Clean pollen grains and BAPr were characterized with a Zeiss Ultra-60 FE-SEM to reveal the morphology. Ethanol suspensions of the pollen grains were deposited by simple drop-casting and dried on silicon wafers at ambient conditions. Then, the silicon wafers were mounted on metal stubs using carbon tape and sputtered with Au/Pd in a Hummer sputtering system to prevent charge build-up during measurement. Scanning electron microscopy (SEM) was also performed on AFM probes before and after mechanical measurements to examine the radii of probe tips. The probes were mounted on metal stubs with carbon tape. The sputtering process was not conducted on the probes so that they could be used for the AFM measurement. All images were obtained under an accelerating voltage of 5.0 or 10.0 kV.

2.4. Peak force quantitative mechanical properties mapping

The elastic moduli of pollen grains were characterized with a PFQNM mode on a Dimension ICON AFM (Bruker). Similar to the tapping mode, peak force (PF) tapping intermittently brings the probe and sample together to contact the surface for a short period at a high frequency (1–2 kHz). Unlike the tapping mode, where the amplitude of the cantilever vibration is kept constant, PF tapping controls the maximum force (i.e. the peak force) on the tip. The conventional tapping mode is used mainly for imaging topography or qualitatively characterizing mechanical properties based on differences in phase response. However, the PF tapping mode analyses f–d curves at every imaging pixel simultaneously, resulting in the capability to determine quantitative adhesion, modulus and energy dissipation information. This allows measurement of the latter data with the same lateral resolution as a topographical image, which is suitable to assess the mechanical properties of micrometre-sized pollen shells [23,24].

Figure 1*a* demonstrates what happens during the interaction between the probe tip and a clean ragweed pollen, using data based on the RTESPA-300 probe and CPr. When the modulation frequency of the cantilever is about 1 Hz, the time from point A to point E is about 1 ms, which enables fast scanning of thousands of contacts between the probe and the sample. As the tip is far away from the sample (point A), there is little or no force on the tip. When approaching the sample, the tip is pulled down to the surface of the sample (point B) by attractive forces (usually van der Waals) as represented by a negative force (below the horizontal dashed line). The tip stays on the surface and the force increases until the z position of the probe reaches the bottom-most position at point C, where the peak force occurs. Then, the probe starts to withdraw and the force decreases until the pull-off point (point D), where the adhesion can no longer hold the tip. Once the tip detaches from the surface, the cantilever oscillates for a period and the force is small or zero (point E). Figure 1*b* shows the same data as figure 1*a* but with the force plotted as a function of the vertical position. This plot can be compared directly with the f–d curve that has been used by many researchers. The f–d curve must be converted to the force–separation (f–s) curve (figure 1*c*) to retrieve the mechanical properties, according to the following equations and figure 1*d*.

$$\Delta x = \frac{F_{\text{tip}}}{k} \tag{2.1}$$

and

$$\Delta d = \Delta z - \Delta x. \tag{2.2}$$

In the above equations, Δx is the deflection of the cantilever, F_{tip} is the loading force applied on the sample by the probe, k is the spring constant of the cantilever, Δd is the deformation of the sample and Δz is the distance of the movement of the probe. In figure 1*c*, the withdrawal curve can be fitted with an appropriate model to obtain the elastic modulus.

In the PFQNM mode, the elastic or Young's modulus is calculated by using the Derjaguin–Muller–Toropov (DMT) model to fit the withdrawal portion of the f–s curve [31]. This model is appropriate when deformation of the sample is lower than the tip radius, which is the case presented here. Therefore, the DMT model is more suitable for hard materials than the classical Hertz model and the Johnson–Kendall–Roberts (JKR) model [29,32]. The reduced Young's modulus, E_{r}, is given by

$$E_{\text{r}} = \frac{3(F_{\text{tip}} - F_{\text{adh}})}{4\sqrt{R(\Delta d)^3}}, \tag{2.3}$$

where F_{adh} is the adhesive force at point D (negative value) and R is the radius of the AFM tip. The tip radius is calibrated by using SEM, a tip calibration grating and standard samples, as discussed in detail in the following section. The reduced elastic modulus is related to the sample elastic modulus, E_{s}, by

$$E_{\text{r}} = \left[\frac{1 - v_{\text{s}}^2}{E_{\text{s}}} + \frac{1 - v_{\text{tip}}^2}{E_{\text{tip}}}\right]^{-1}, \tag{2.4}$$

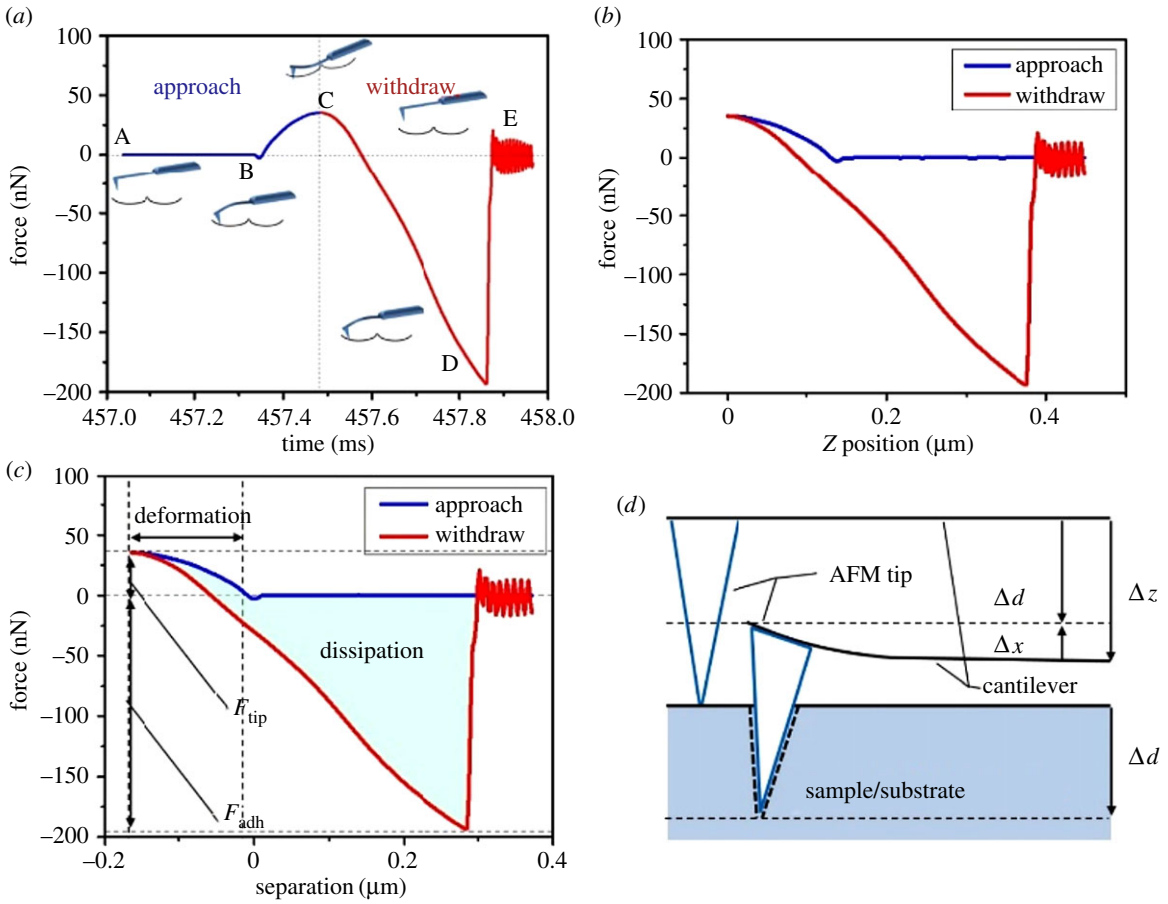

Figure 1. (*a*) Plot of force as a function of time for RTESPA-300 interacting with CPr; the insets are probe–sample interactions at different points of the plot, including point (B) jump-to-contact, (C) peak force, (D) pull-off and (E) free oscillation of the probe after surface detachment. (*b*) Plot of force as a function of *z* (vertical) piezo position. (*c*) Plot of force as a function of probe–sample separation distance. (*d*) An illustration of the relationship between probe deflection (Δx) of the probe and sample deformation (Δd). (Online version in colour.)

Table 1. AFM probes used in this work.

probe type	tip material	nominal spring constant (N m^{-1})	sample modulus	reference sample (nominal modulus)
RTESPA-300	silicon	40	0.2–2 GPa	PS (2.7 GPa)
RTESPA-525	silicon	200	1–20 GPa	HOPG (18.0 GPa)

where ν_s and ν_{tip} are Poisson's ratios of the sample and the AFM tip, respectively. In this work, we assume that E_{tip} is much larger than E_s, and so, the second term on the right-hand side of equation (2.4) is negligible. For typical values of the silicon modulus (170 GPa) and Poisson ratio (0.22) [33], over the range of moduli values determined below for E_s, this assumption creates 2–7% difference between E_r and E_s. Poisson's ratio of polymers generally ranges between 0.2 (very rigid) and 0.5 (rubber), which gives a 4%–25% difference between E_r and E_s [34]. As we assume that pollen shells have a similar Poisson's ratio to rigid polymers, based on the heavily cross-linked structure of sporopollenin, ν_s is set to be 0.35 for the pollen shells in this work. All calculations are done in real time for every f–s curve over the scanned area.

For each measurement, a 5 × 5 μm^2 area was scanned by the probe, resulting in 512 × 512 f–s curves, and the average modulus was calculated based on these individual measurements. A larger magnification (smaller area) was investigated when artefacts were detected due to the morphology effect, which is discussed in detail in the Results section. Five pollen grains were measured for each species, and two to four measurements were taken from each pollen grain. Each measurement generates an image containing 256 by 256 pixels. All measurements were conducted at 24% RH and 20°C.

2.5. Probe selection

Considering the pollen shell as a rigid material, probes require a stiff cantilever to apply sufficient force to indent the sample. Two types of Bruker AFM probes, RTESPA-300 and RTESPA-525, were selected to cover the modulus range from 200 MPa to 20 GPa. Table 1 shows some specifications of the probes. The spring constant (k) and tip radius (R) of probes were determined through a combination of absolute and relative calibration methods.

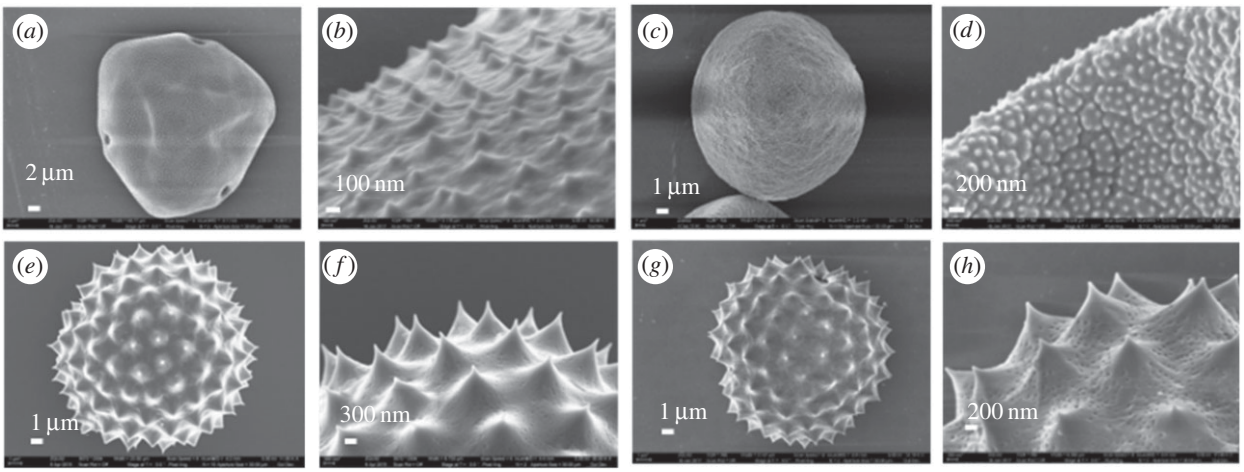

Figure 2. SEM images of the clean pollen shells of (*a*,*b*) pecan (CPp); (*c*,*d*) Kentucky bluegrass (CPk); (*e*,*f*) ragweed (CPr), and (*g*,*h*) base–acid-treated ragweed pollen (BAPr).

2.6. Probe calibration

Both absolute and relative calibration methods are used to obtain probe parameters for PFQNM. Based on equations (2.1) and (2.3), E_r is proportional to $k/(R^{1/2})$. The absolute method gives a direct measurement of R and k. By contrast, the relative method uses a reference sample with known elastic modulus to acquire the ratio of $k/(R^{1/2})$. A combination of both methods was used in this work to ensure the accuracy of the calibration. Both methods require measurement of the deflection sensitivity on a hard sample. In this work, a sapphire sample (SAPPHIRE-12M) from the PFQNM sample kit was used to obtain the deflection sensitivity. Then, the spring constant was calculated using Sader's method [30], where the dimensions of the cantilever were obtained using SEM, and the resonant frequency and Q factor were obtained using the thermal tuning function of the AFM. The tip radii before and after AFM measurements were obtained by SEM. The tip radii were also calibrated on a tip characterization sample, RS-12M, from the PFQNM sample kit. For the relative method, polystyrene (PS) and highly oriented pyrolytic graphite (HOPG) films were used as the reference samples (table 1). Although the nominal elastic modulus of PS slightly exceeds the suggested modulus range for RTESPA-300, it is close to the upper limit. Furthermore, the relative method requires that the deformation of the measured samples should be consistent with the deformation of the reference sample. According to the instrument manufacturer, the deformation of both the reference sample and the unknown samples are required to be larger than 2 nm and must be comparable with the deflection of the probe cantilever ($0.3 \times$ deflection $<$ deformation $< 3 \times$ deflection) [23]. Otherwise, the probe will be too stiff or too soft for the given samples, which can lead to cumulative errors in following model fitting. In addition, because data from PFQNM are a distribution, a MATLAB code was developed and used to rule out data not conforming to these deformation guidelines.

3. Results and discussion

3.1. Pollen morphology

SEM images of CPr, CPp, CPk and BAPr are shown in figure 2. Grooves and tiny pores can be observed, demonstrating that the pollenkitt has been eliminated by washing with the methanol/chloroform mixture. Base–acid treatment does not have a significant impact on the morphology. The dimensions of the pollen grains are shown in table 2. CPp has small bumps sparsely distributed on the surface. While CPr and BAPr have very large spines and tiny pores, CPk also has similar bumps to CPp, but the bumps of CPk are much denser than those of CPp. In addition, CPp and CPk sometimes have folded or collapsed shells. Features including spines, pores, bumps and folds were carefully avoided in AFM measurement and the results below are based on relatively flat, featureless areas.

Table 2. Dimensions of pollen grains.

type	diameter (µm)	length of spine (nm)	radius of spine (nm)
CPp	38 ± 2	190–240	45 ± 4
CPk	26 ± 3	80–130	57 ± 12
CPr	15 ± 3	500–1000	52 ± 5
BAPr	15 ± 3	500–1000	52 ± 5

3.2. Probe calibration

Figure 3 shows SEM images of the RTESPA-525 AFM probes at various times during the measurement stage. The dimensions, resonant frequency and Q factor were used to calculate the spring constants (k) with Sader's method ('absolute' technique). This method was reported to have the least uncertainty, which mainly comes from the errors of measurement of the cantilever width [35]. Table 3 shows the tip radii measured with the different methods before and after measuring five pollen grains. Before the AFM measurements of pollen samples, the difference in radii comparing the SEM images to the results of absolute or relative calibration is due to wear that occurred during the calibration. The discrepancy between the absolute method and the relative method is mainly because of the imperfect tip shape, which deviates from the spherical tip shape assumption of the DMT model. However, after measuring five pollen grains, SEM

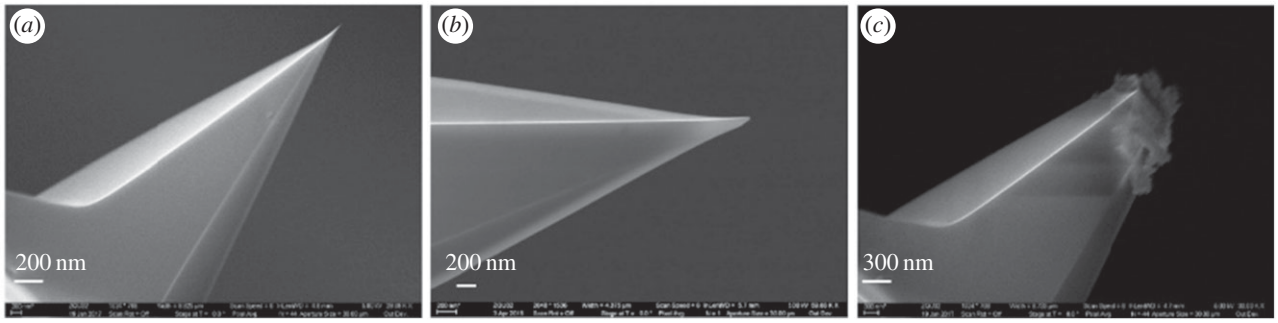

Figure 3. SEM images of RTESPA-525: (*a*) new probe, (*b*) after calibration on HOPG; (*c*) after measurements on five pollen grains.

Table 3. Tip radii measured or estimated by different methods before and after AFM measurement of pollen.

	probe	SEM (nm)	absolute method (nm)	relative method (nm)
before	RTESPA-300	10 ± 0.15	20.7 ± 2.1	50 ± 7.6
	RTESPA-525	10 ± 0.11	23.4 ± 1.8	60 ± 3.6
after	RTESPA-300	n.a.	n.a.	160 ± 30
	RTESPA-525	480 ± 165	n.a.	210 ± 20

images show much higher tip radii than the results measured with the relative method. This is because only a small portion of the blunt tip is in contact with the sample during AFM measurement, and this contacting radius is what is relevant to the measurement of modulus values. After measuring each individual pollen grain, the probe was indented on the PS or HOPG sample again to check for drift in the modulus measured for the reference sample, which could indicate a change in tip size. If the average moduli of PS or HOPG were consistent with the nominal value, the probe was used to measure the next pollen grain. Otherwise, the tip radius was adjusted in the software to match the measured moduli of PS or HOPG with the reference modulus values. Figure 4 shows the measured moduli of PS and HOPG before and after the tips were used to characterize five pollen grains. The measured moduli of PS and HOPG drifted from initial values of 2.67 and 17.8 GPa to final values of 3.14 and 23.4 GPa at the end of all measurements, due to the wear on the tip. SEM confirmed the wear on the tip that occurs after measuring five pollen grains (figure 3*c*,*d*). The more blunt tips lead to a shorter indentation depth (d) and the calculated modulus will be artificially higher according to equation (2.3). Correcting the tip radius to achieve the nominal modulus value accounts for changes in tip radius during measurement. By contrast, the surfaces of the calibration standards and the pollen do not show wear following indentation measurements.

3.3. Excluding curved morphologies with data analysis

In preliminary experiments, the RTESPA-300 probe was used to scan $5 \times 5\ \mu m^2$ areas on CPp, CPk, CPr and BAPr by AFM. Multiple channels were recording the topological and mechanical properties of the sample in real time. For example, figure 5 shows the height, three-dimensional (3D) height, adhesion, deformation and modulus maps of BAPr. The 3D height image shows four intact spines, as well as several half spines at the edges. Moreover, tiny pores and grooves on the pollen surface can even be observed from the 3D height and deformation images. Correlations can be found between the height images and the other mechanical property maps. For the deformation image, the area surrounding the tips of spines showed larger deformation (lighter colour on the map) than the other areas. Consequently, the moduli of those areas were much lower than the other areas according to equation (2.3). This contrast is more likely due to the spiny morphology rather than the intrinsic heterogeneity of the moduli of pollen shell. As shown in figure 5*f*, the surface near the tip of the spine was much steeper compared to the horizontal surface between spines. When the probe taps this steep surface, it is easy to slip down the surface. The slip can only happen after contact point (point B in figure 1*a*), and thus, the slipping distance will be mistakenly accounted for as deformation of the sample by the DMT model. In addition, the DMT model assumes that the interaction is between a sphere and a flat surface. Thus, the DMT model does not hold when the tip is tapping the steep surfaces around the spines. Adhesion maps also showed remarkable correlations with the spiny morphology.

The adhesion forces at the area surrounding the tip of the spine are much higher than those at the tip of the spine and the spacing between spines. This may be due to the difference in contact areas formed at different locations. When the probe taps near the apex of the spine, it makes contact over a relatively small area near the probe tip. However, when the probe taps the steep side surface around the spine's apex, it could achieve a much larger contact area by contacting with the spine side-by-side. Therefore, the adhesion forces around the spine apex could be larger than those at the apex or the space between spines. It is noted that large adhesion forces were also observed at some grooves or pores of the pollen shell. This could also be due to the larger contact areas formed when the probe taps and even inserts into those specific morphologies. Similar

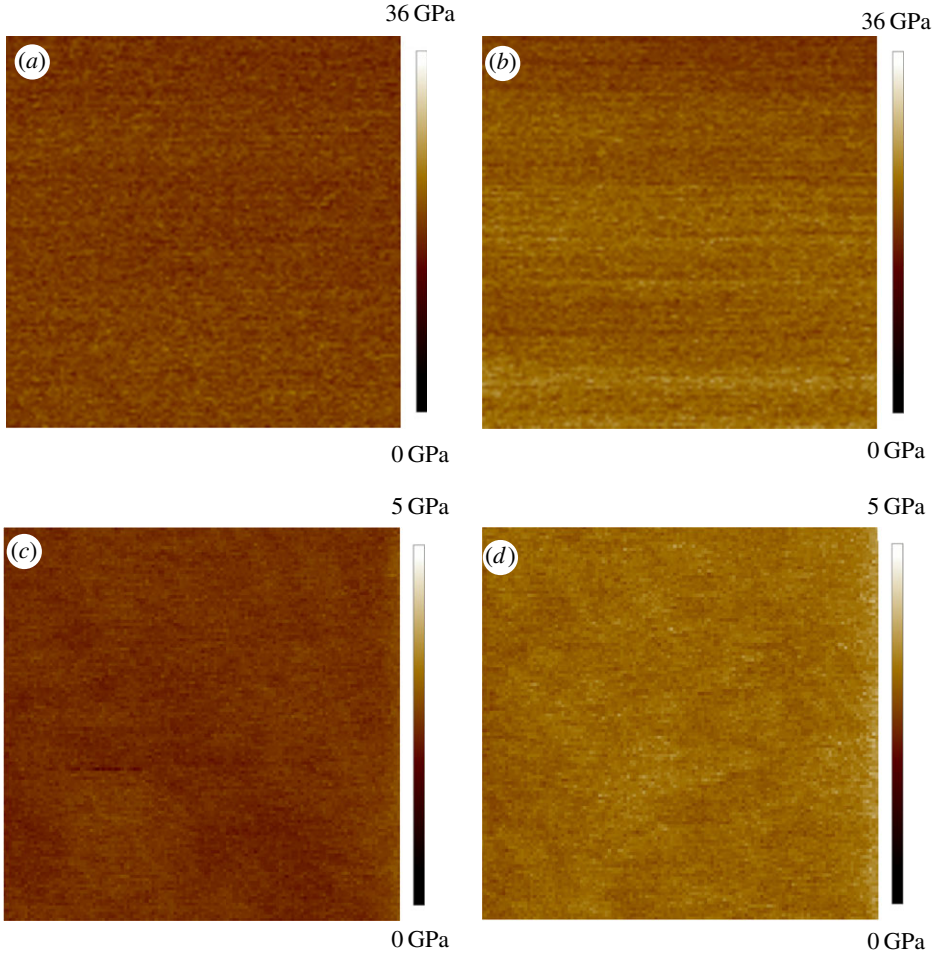

Figure 4. The moduli maps of (*a*) HOPG with new RTESPA-525, (*b*) HOPG with used RTESPA-525, (*c*) PS with new RTESPA-300 and (*d*) PS with used RTESPA-300; all images are 100 nm × 100 nm. (Online version in colour.)

morphology effects were also reported in the literature for modulus mapping of individual chitin nanorods with PFQNM [32].

The other three types of pollen also showed similar morphology effects on the mechanical characterization. Although CPp and CPk (figure 2) have less morphology effect due to their smaller bumps than ragweed pollen, the modulus data over spines and bumps are not included in the following data analysis, to avoid potential artefacts caused by the morphology issue. After a $5 \times 5\ \mu m^2$ area was scanned first to give a morphology map, smaller portions of the $5 \times 5\ \mu m^2$ area without spines or bumps were rescanned to obtain mechanical properties.

3.4. Probe effect

The elastic moduli of pollen shells are still largely unexplored in the literature. Only one paper reported the product of the Young's modulus and wall thickness ($E \cdot h$) of desiccated ragweed pollen as $1653 \pm 36\ N\ m^{-1}$ [19]. This value is based upon the mean rupture force and deformation of the ragweed pollen under compression. An accurate average modulus can be obtained only if the wall thickness is known accurately. If the thickness of the pollen shell is taken to be approximately 1 μm based upon SEM images in the literature, Young's modulus will be about 1.6 GPa [2]. Therefore, the RTESPA-300 probe, with a suggested sample modulus of 20–2000 MPa, was chosen for the characterization. Figure 6*a* shows the average elastic moduli of CPp, CPk, CPr and BAPr measured by using RTESPA-300. BAPr has the lowest modulus of 1.46 ± 0.38 GPa, while CPr shows a much higher modulus of 8.45 ± 0.43 GPa without base–acid treatment. CPk and CPp show relatively large moduli of 8.70 ± 1.15 GPa and 7.54 ± 2.72 GPa, respectively. The smaller sample size of CPr and BAPr is due to the morphology of ragweed pollen. The long spines make it difficult to get usable data on every ragweed pollen. It is noted that all results except for BAPr exceed the suggested moduli range of RTESPA-300. Moreover, most of the deformation data of these samples are below 2 nm. Small deformation indicates that RTESPA-300 is too soft to make a significant indentation on the pollen shell. Therefore, RTESPA-300 is not a suitable probe for CPr, CPp and CPk.

As RTESPA-300 was not appropriate, a stiffer probe, RTESPA-525, was used for AFM measurement. Figure 6*a* shows the moduli of the pollen grains measured by RTESPA-300 and RTESPA-525, respectively. The moduli measured by RTESPA-525 are between 1 and 20 GPa, which is the suggested sample moduli range of the probe. The deformations are sufficient and comparable with the deflections for fitting the DMT model (figure 6*b*). Hence, the results from RTESPA-525 were more reliable than those from RTESPA-300. Overall, higher elastic moduli were obtained with RTESPA-525 for CPp and CPk. With RTESPA-525, the average moduli of CPr, CPk and CPp are 16.2 ± 2.45 GPa, 16.1 ± 3.96 GPa and 9.53 ± 2.33 GPa, respectively. Thus, the moduli of CPr, CPk and CPp are

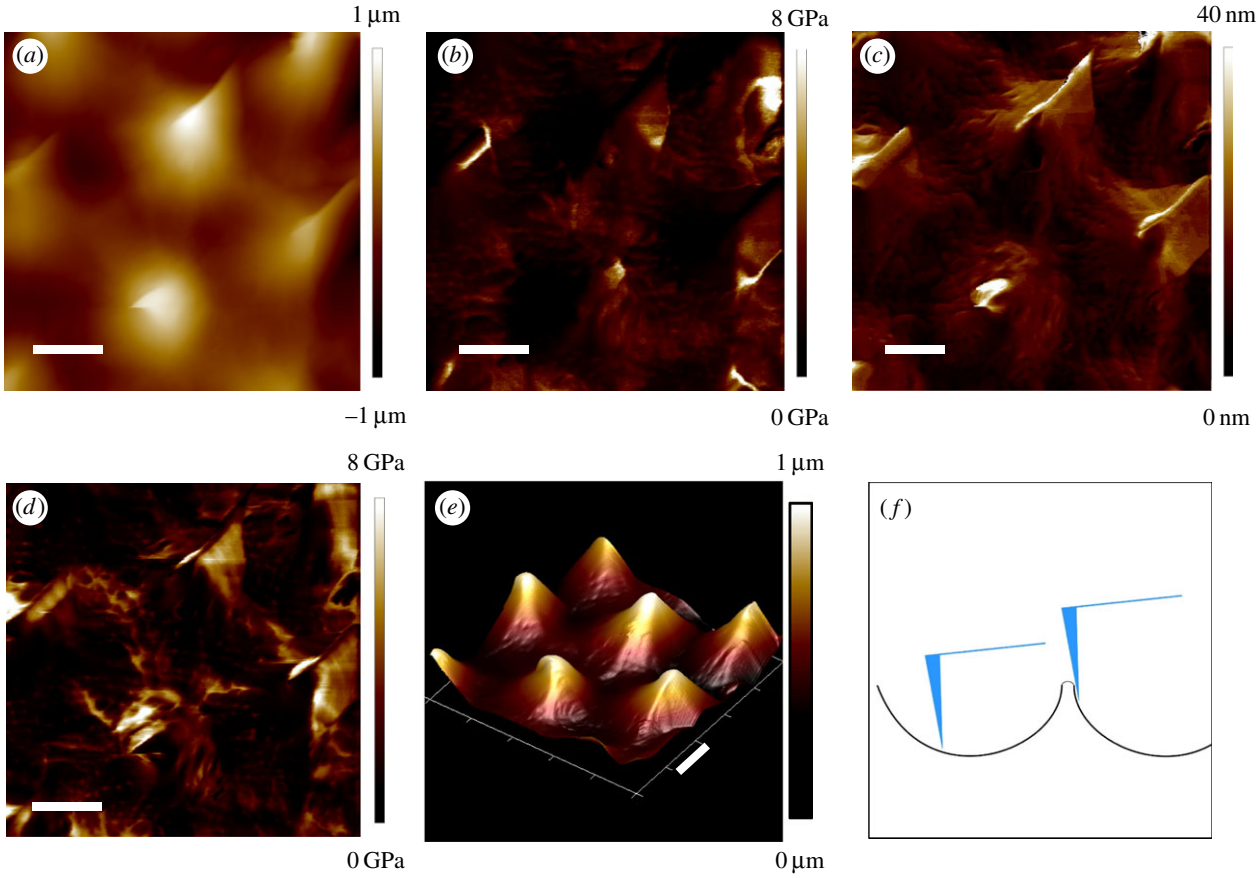

Figure 5. AFM images of BAPr: (*a*) height, (*b*) modulus, (*c*) deformation, (*d*) adhesion, (*e*) 3D height and (*f*) an illustration of the probe–pollen interaction. The scale bar is 1 µm. (Online version in colour.)

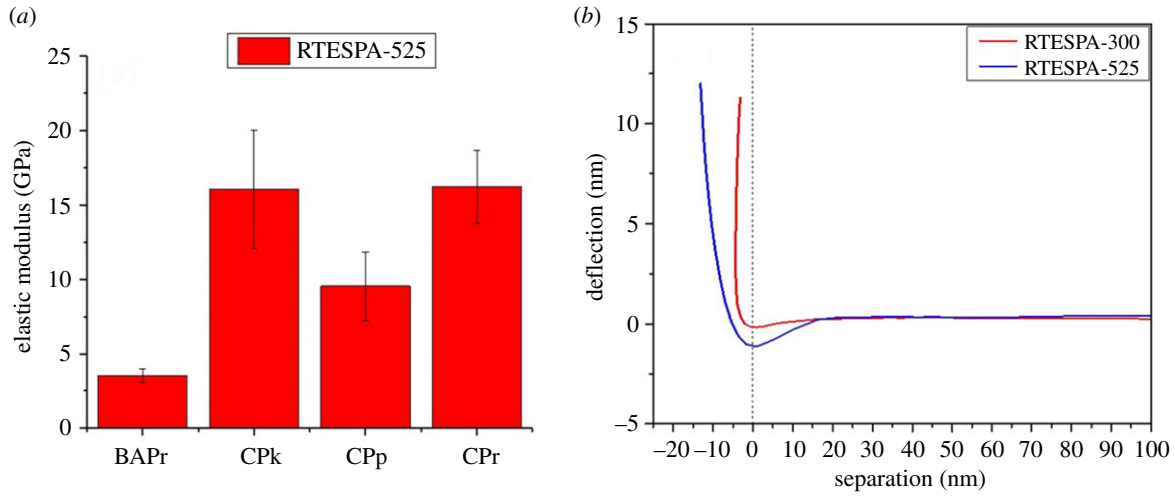

Figure 6. (*a*) The average moduli of BAPr, CPk, CPp and CPr by RTESPA-500. (*b*) The deflection versus separation curves of RTESPA-300 and RTESPA-525 used to fit the DMT model; data were taken with a clean ragweed pollen as a representative. (Online version in colour.)

even higher than most non-reinforced polymers [36]. It is interesting that the moduli are close to the elastic moduli of phenolic plastics, and phenolic compounds were found in sporopollenin [37]. The high elastic moduli indicate the great potential of pollen shells to be used as a polymer reinforcing filler with the advantages such as low density, low cost, bio-renewability and ready surface modification [2]. It is noted that these two types of probes give similar results for CPp with a difference of 2 GPa, as well as overlapped error bars. It indicates that RTESPA-300 could be used for some samples (CPp) with higher moduli than the range suggested by Bruker, even though RTESPA-525 is a better choice in this work.

3.5. Effect of base–acid treatment

Both RTESPA-300 and RTESPA-525 gave higher moduli for CPr compared with BAPr. The moduli of BAPr decreased by 58.4% and 47.9% using RTESPA-300 and RTESPA-525, respectively. The results indicate that the base–acid treatment can reduce the stiffness of pollen shells by about 50%, while the morphology can be maintained. Synthetic polyester

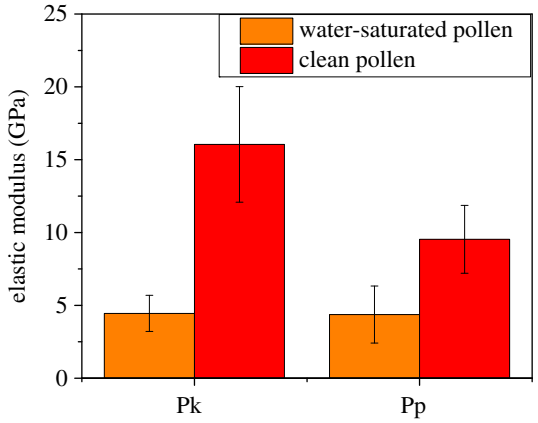

Figure 7. The average moduli of WSPk and WSPp compared with the moduli of CPk and CPp. (Online version in colour.)

polymer has been reported to show a similar effect with respect to acid–alkali treatment, where the Young's modulus of polyester fibre was reduced by 41% (acid treated) and 28% (alkali treated) [38]. Considering the cross-linked structure of sporopollenin by ester bonds, this reduction is presumed to be due to the degradation of the macromolecular network through hydrolysis. Although the base–acid treatment can reduce the elastic moduli of pollen shells, BAPr shows higher moduli than some common polymers. Therefore, BAPr can still be useful for reinforcing polymer matrices, which is important because the base–acid treatment has been shown to facilitate the surface modification of pollen shells and their compatibility with polymers. This is consistent with the results of Fadiran *et al*. who used AB treatment of Pr as a precursor to silanization of pollen with vinylsilane coupling agents to prepare Pr-poly(vinyl acetate)-reinforced composites [2].

3.6. Effect of water vapour exposure

In a previous work by Lin *et al*. [39], it was shown that cleaned ragweed pollen can become saturated with water as the humidity is raised, through both adsorption and absorption. It was found that ragweed gained water in the amount of 16% dry mass at a humidity of 70%. As described above, ragweed pollen are more difficult to characterize using AFM than pecan and Kentucky bluegrass due to the spiny morphology. Therefore, only CPp and CPk were used to investigate the effect of exposure to water via elevated humidity. The same samples of CPp and CPk that were measured previously by the RTESPA-525 tip at normal room humidity were stored in a 90% RH environment for 24 h. Then, the resulting water-saturated pecan and Kentucky bluegrass pollen (WSPp and WSPk) were measured quickly with AFM while holding RH at 24% RH to avoid water condensation during measurements. WSPp and WSPk were also re-saturated at 90% RH every 30 min during the experiment. Figure 7 shows the average moduli of WSPp, CPp, WSPk and CPk measured with probe RTESPA-525. CPp and CPk show average moduli higher than 10 GPa. However, both WSPp and WSPk show reduced moduli of 4.37 ± 1.96 GPa and 4.45 ± 1.24 GPa, respectively. In comparison with those of CPp and CPk, these values correspond to a decrease of 54.1% (WSPp) and 72.3% (WSPk), a result that indicates that while water saturation reduced the stiffness of the pollen shells, the moduli still exceed 4 GPa. The topological image (figure 8) of WSPk also showed a different morphology compared with CPk. WSPk has a relatively smooth surface compared to CPk, which may be due to levelling of bumps following the swelling of the sporopollenin with water.

One concern for the experiment is whether absorbed water will affect PFQNM by introducing capillary adhesion. At high humidity (70% RH), the water taken up by the pollen exine is mainly absorbed by the bulk sporopollenin according to Lin *et al*. [39]. Only 25% of water is adsorbed on the surface or condensed in small cavities. However, in this work, pollen shells are only pre-stored in high humidity. The experiments were still conducted in air a 24% RH, where additional water condensation between the tip and pollen is unlikely [40]. Moreover, the loading force of the cantilever is 1–2 μN, while the capillary force is only tens of nano-newtons at the most. In other words, even if a capillary or pendular bridge is formed in the probe–sample interaction, it will only have a small effect on the modulus measurement according to equation (2.3).

3.7. Comparison with other biomaterials

As a non-crystalline material, sporopollenin showed a surprisingly high elastic modulus under dry conditions, comparing with other amorphous, neat biomaterials. Table 4 shows the Young's moduli of several biomaterials, including protein fibres from animals, hemicellulose and lignin from plants. In general, the plant polymers show higher Young's moduli than the animal ones. Under dry conditions, sporopollenin has the highest Young's moduli, 16.2 GPa for ragweed and Kentucky Bluegrass, and 9.53 GPa for pecan. The second highest moduli are 6.7 GPa (lignin) and 6.0 GPa (β-glucan), which are 2.7 and 2.4 times less than ragweed pollen exine. Animal proteins (actin, tubulin and collagen) and arabinoxylan have the lowest Young's moduli between 1 and 3 GPa. It is worth noting that sporopollenin bears some resemblance to lignin. Lignins are a class of complex aromatic, hydroxylated polymers that act as a binder for cellulose in plants and algae. Both sporopollenin and lignin have similar precursors (ferulic acid and phenylalanine) and phenolic ester/ether cross-linking. In addition, lignin has a similar response to elevated water content as sporopollenin. The Young's modulus of lignin decreased by 54% (from 6.7 to 3.1 GPa), when the water content increased from 3.2 to 12 wt%. Meanwhile, the moduli of pecan and Kentucky bluegrass pollen exine decreased by 54.1% and 72.3%, when the environment's RH increased from 24% to 90%. In addition, the hydration effect of pollen exine indicates the amorphous structure of sporopollenin, which is already confirmed with X-ray diffraction [41].

3.8. Implications in the natural world and materials science

Implications of the high modulus of sporopollenin in the natural world relate to the protective effect for generative cells offered by the very stiff external shell. Under natural loading forces, the high stiffness prevents significant compression of the internal cells, preserving their reproductive function. Even after extended exposure to elevated humidity of 90%, the exine retains a relatively high modulus over 4 GPa, indicating an important ability to continue to provide resistance to deformation under wide swings in

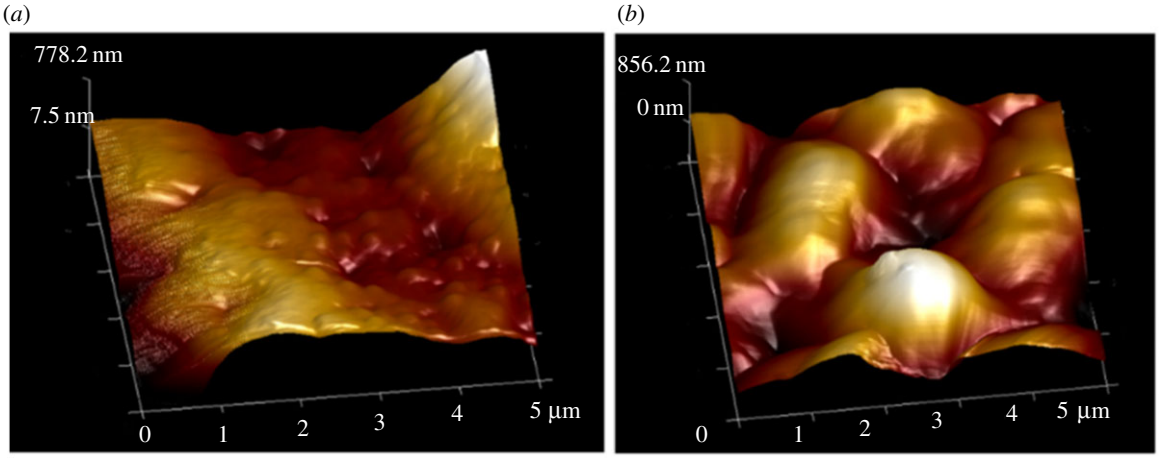

Figure 8. Three-dimensional-height images of (*a*) CPk and (*b*) WSPk by RTESPA-525. (Online version in colour.)

Table 4. Young's modulus of representative biomaterials.

material	Young's modulus (GPa)	method	reference
actin	1.8	nanomanipulation	[43]
tubulin	1.2	thermal fluctuation	[44]
lignin	6.7 (3.2% water) 3.1 (12% water)	tensile test	[42]
hemicelluloses			
arabinoxylan	1.3, 2.9	tensile test	[45,46]
β-glucan	6.0	tensile test	[47]
collagen	2.7, 4.59	AFM manipulation	[48,49]
sporopollenin	9.5–16 (24% RH) 4.4 (90% RH)	AFM PFQNM	this work

humidity. A second natural effect of the stiffness, beyond protection of the germ cell contents, is the influence of spine stiffness on pollen adhesion. For example, prior work has shown that pressing spiny sunflower pollen into a sunflower stigma results in a pressure-dependent interlocking effect between pollen spines and complimentary hair-like features on the stigma [16]. If the spines were significantly softer and compliant, the interlocking would likely not occur. In nature, an oily plant-derived pollenkitt film is present on many pollens. In our studies, the pollenkitt liquid film has been removed in order to prevent the formation of capillary bridges with the indenter tip and so that it does not prevent the hydration of pollen in our elevated humidity experiments. There is a possibility that the pollenkitt could soften the exine to some extent, acting as a plasticizer, if it is solubilized in the sporopollenin. We cannot rule out this whether the oily pollenkitt is absorbed, to some extent, in the exine and this would be a useful subject for future study. The high modulus of sporopollenin supports material applications of pollen exine that have begun to emerge, especially the use of pollen to reinforce polymer composites where the modulus of the pollen directly increases the modulus of the composites [2,3]. In vaccine or drug delivery [4,5], a high modulus will support retention of shape and preservation of release characteristics *in vivo*.

4. Conclusion

For the first time, the elastic moduli of three types of pollen exine (shells) were measured directly by using AFM peak force quantitative nanomechanical mapping. Kentucky blue grass and ragweed pollens had moduli of 16 GPa, while pecan particles had a lower modulus between 8 and 10 GPa. In addition, sporopollenin was observed to be a very tough material qualitatively and did not sustain any visible damage by SEM inspection even after multiple indentations with much stiffer silicon AFM tips. By contrast, silicon AFM tips were readily abraded after indentation on sporopollenin. A base–acid treatment, which is commonly used to clean, and process pollen, reduced the modulus of ragweed pollen from 16 ± 2.5 to 3.5 ± 0.5 GPa. Furthermore, water vapour saturation at elevated humidity of 90% decreased the moduli of pecan and Kentucky blue grass pollens by 54.1% and 72.3%, respectively. This sensitivity is consistent with prior observations of water absorption by sporopollenin [39] and is similar to that observed for other natural amorphous biological materials [42]. In addition, AFM images indicate the swelling of sporopollenin after water vapour exposure. Overall, we conclude that that sporopollenin is an unusually stiff biomaterial, with a modulus that exceeds most other non-crystalline biomaterials. High stiffness likely supports the protective effects of the pollen

exine for internal germ cells as well as adhesive functions of pollen exine, particularly when pollen are pressed onto other patterned substrates. For example, it was shown recently that pollen spines can lock onto similarly sized features on flower stigma surfaces, resulting in pressure-dependent adhesion behaviour. Stiff sporopollenin features support the appearance of load-dependent frictional forces as stigma hairs are forced in between the pollen spines. These results also indicate the potential of pollen particle exine shells as relatively stiff materials that can be used in applications such as reinforcing fillers for polymers [2,3] and protective shells for sensitive materials such as drugs [4–6].

Data accessibility. The data can be obtained from: https://smartech.gatech.edu/handle/1853/58846.

Authors' contributions. Z.Q. conceived of the study, designed the study and carried out all laboratory work. J.C.M. contributed to data analysis and interpretation as well as preparation of the manuscript. All authors gave final approval for publication.

Competing interests. The authors declare no competing financial interest.

Funding. We gratefully acknowledge financial support from the Air Force Office of Scientific Research (grant no. FA9550-10-1-0555).

Acknowledgements. The authors thank Dr Elsa Reichmanis and Dr John Reynolds for providing atomic force microscopy (Dimension ICON), Dr Zifu Li and Dr Haisheng Lin for their valuable comments.

References

1. Lin H, Gomez I, Meredith JC. 2013 Pollenkitt wetting mechanism enables species-specific tunable pollen adhesion. *Langmuir* **29**, 3012–3023. (doi:10.1021/la305144z)
2. Fadiran OO, Meredith JC. 2014 Surface treated pollen performance as a renewable reinforcing filler for poly(vinyl acetate). *J. Mater. Chem. A* **2**, 17 031–17 040. (doi:10.1039/C4TA03219E)
3. Fadiran OO, Girouard OO, Meredith JC. 2018 Pollen fillers for reinforcing and strengthening of epoxy composites. *Emergent Mater.* in press. (doi:10.1007/s42247-018-0009-x)
4. Uddin MJ, Gill HS. 2017 Ragweed pollen as an oral vaccine delivery system: mechanistic insights. *J. Control Release* **268**, 416–426. (doi:10.1016/j.jconrel.2017.10.019)
5. Uddin MJ, Gill HS. 2018 From allergen to oral vaccine carrier: a new face of ragweed pollen. *Int. J. Pharm.* **545**, 286–294. (doi:10.1016/j.ijpharm.2018.05.003)
6. Diego-Taboada A, Beckett S, Atkin S, Mackenzie G. 2014 Hollow pollen shells to enhance drug delivery. *Pharmaceutics* **6**, 80–96. (doi:10.3390/pharmaceutics6010080)
7. Gomez IJ, Goodwin WB, Sabo D, Zhang ZJ, Sandhage KH, Meredith JC. 2015 Three-dimensional magnetite replicas of pollen particles with tailorable and predictable multimodal adhesion. *J. Mater. Chem. C* **3**, 632–643. (doi:10.1039/C4TC01938E)
8. Goodwin WB, Donglee S, Daniel S, Sunghwan H, Zhang ZJ, Meredith JC, Kenneth HS. 2017 Tunable multimodal adhesion of 3D, nanocrystalline $CoFe_2O_4$ pollen replicas. *Bioinspir. Biomim.* **12**, 066009. (doi:10.1088/1748-3190/aa7c89)
9. Lin H, Allen MC, Wu J, deGlee BM, Shin D, Cai Y, Sandhage KH, Deheyn DD, Meredith JC. 2015 Bioenabled core/shell microparticles with tailored multimodal adhesion and optical reflectivity. *Chem. Mater.* **27**, 7321–7330. (doi:10.1021/acs.chemmater.5b02782)
10. Johnstone LR, Gomez IJ, Lin H, Fadiran OO, Chen VW, Meredith JC, Perry JW. 2017 Adhesion enhancements and surface-enhanced Raman scattering activity of Ag and $Ag@SiO_2$ nanoparticle decorated ragweed pollen microparticle sensor. *ACS Appl. Mater. Interfaces* **9**, 24 804–24 811. (doi:10.1021/acsami.6b15664)
11. Piffanelli P, Ross JHE, Murphy DJ. 1998 Biogenesis and function of the lipidic structures of pollen grains. *Sexual Plant Reprod.* **11**, 65–80. (doi:10.1007/s004970050122)
12. Brooks J, Shaw G. 1978 Sporopollenin: a review of its chemistry, palaeochemistry and geochemistry. *Grana* **17**, 91–97. (doi:10.1080/00173137809428858)
13. Mackenzie G, Boa AN, Diego-Taboada A, Atkin SL, Sathyapalan T. 2015 Sporopollenin. The least known yet toughest natural biopolymer. *Front. Mater.* **2**, 1–5. (doi:10.3389/fmats.2015.00066)
14. Domínguez E, Mercado JA, Quesada MA, Heredia A. 1999 Pollen sporopollenin: degradation and structural elucidation. *Sexual Plant Reprod.* **12**, 171–178. (doi:10.1007/s004970050189)
15. Chiappe C, Demontis GC, Di Bussolo V, Rodriguez Douton MJ, Rossella F, Pomelli CS, Sartini S, Caporali S. 2017 From pollen grains to functionalized microcapsules: a facile chemical route using ionic liquids. *Green Chem.* **19**, 1028–1033. (doi:10.1039/C6GC02892F)
16. Lin H, Qu Z, Meredith JC. 2016 Pressure sensitive microparticle adhesion through biomimicry of the pollen-stigma interaction. *Soft Matter* **12**, 2965–2975. (doi:10.1039/c5sm02845k)
17. Watson GS, Cribb BW, Schwarzkopf L, Watson JA. 2015 Contaminant adhesion (aerial/ground buifouling) on the skin of a gecko. *Journal of the Royal Society Interface* **12**, 20150318. (doi:10.1098/rsif.2015.0318)
18. Katifori E, Alben S, Cerda E, Nelson DR, Dumais J. 2010 Foldable structures and the natural design of pollen grains. *Proc. Natl Acad. Sci. USA* **107**, 7635–7639. (doi:10.1073/pnas.0911223107)
19. Liu T, Zhang Z. 2004 Mechanical properties of desiccated ragweed pollen grains determined by micromanipulation and theoretical modelling. *Biotechnol. Bioeng.* **85**, 770–775. (doi:10.1002/bit.10908)
20. Heinz WF, Hoh JH. 1999 Spatially resolved force spectroscopy of biological surfaces using the atomic force microscope. *Trends Biotechnol.* **17**, 143–150. (doi:10.1016/S0167-7799(99)01304-9)
21. Gaboriaud F, Parcha BS, Gee ML, Holden JA, Strugnell RA. 2008 Spatially resolved force spectroscopy of bacterial surfaces using force–volume imaging. *Colloids Surf. B* **62**, 206–213. (doi:10.1016/j.colsurfb.2007.10.004)
22. Rosa-Zeiser A, Weilandt E, Hild S, Marti O. 1997 The simultaneous measurement of elastic, electrostatic and adhesive properties by scanning force microscopy: pulsed-force mode operation. *Meas. Sci. Technol.* **8**, 1333–1338. (doi:10.1088/0957-0233/8/11/020)
23. Pittenger B, Erina N, Su C. 2010 *Quantitative mechanical property mapping at the nanoscale with PeakForce QNM*. Application Note Bruker Instruments, Inc. AN128, Rev. B0, 1–12. See https://www.bruker.com/fileadmin/user_upload/8-PDF-Docs/SurfaceAnalysis/AFM/ApplicationNotes/AN128-RevB0-Quantitative_Mechanical_Property_Mapping_at_the_Nanoscale_with_PeakForceQNM-AppNote.pdf.
24. Adamcik J, Berquand A, Mezzenga R. 2011 Single-step direct measurement of amyloid fibrils stiffness by peak force quantitative nanomechanical atomic force microscopy. *Appl. Phys. Lett.* **98**. (doi:10.1063/1.3589369)
25. Heu C, Berquand A, Elie-Caille C, Nicod L. 2012 Glyphosate-induced stiffening of HaCaT keratinocytes, a peak force tapping study on living cells. *J. Struct. Biol.* **178**, 1–7. (doi:10.1016/j.jsb.2012.02.007)
26. Pletikapić G, Berquand A, Radić TM, Svetličić V. 2012 Quantitative nanomechanical mapping of marine diatom in seawater using peak force tapping atomic force microscopy. *J. Phycol.* **48**, 174–185. (doi:10.1111/j.1529-8817.2011.01093.x)
27. Xavier P, Bose S. 2016 Nanomechanical mapping, hierarchical polymer dynamics, and miscibility in the presence of chain-end grafted nanoparticles. *Macromolecules* **49**, 1036–1048. (doi:10.1021/acs.macromol.5b01849)
28. Li JXW, Kawashima S, Shekhawat GS, Shah SP. 2015 Experimental investigation on quantitative nanomechanical properties of cement paste.

Mater. J. **112**, 229–238. (doi:10.14359/51686986)

29. Morales-Rivas L, González-Orive A, Garcia-Mateo C, Hernández-Creus A, Caballero FG, Vázquez L. 2015 Nanomechanical characterization of nanostructured bainitic steel: peak force microscopy and nanoindentation with AFM. *Sci. Rep.* **5**, 17164. (doi:10.1038/srep17164)
30. Ducker WA, Senden TJ, Pashley RM. 1991 Direct measurement of colloidal forces using an atomic force microscope. *Nature* **353**, 239–241. (doi:10.1038/353239a0)
31. Derjaguin BV, Muller VM, Toporov YP. 1975 Effect of contact deformations on the adhesion of particles. *J. Colloid Interface Sci.* **53**, 314–326. (doi:10.1016/0021-9797(75)90018-1)
32. Smolyakov G, Pruvost S, Cardoso L, Alonso B, Belamie E, Duchet-Rumeau J. 2016 AFM PeakForce QNM mode: evidencing nanometre-scale mechanical properties of chitin–silica hybrid nanocomposites. *Carbohydr. Polym.* **151**, 373–380. (doi:10.1016/j.carbpol.2016.05.042)
33. Hopcroft MA, Nix WD, Kenny TW. 2010 What is the Young's modulus of silicon? *J. Microelectromech. Syst.* **19**, 229–238. (doi:10.1109/JMEMS.2009.2039697)
34. Sader JE, Chon JW, Mulvaney P. 1999 Calibration of rectangular atomic force microscope cantilevers. *Rev. Sci. Instrum.* **70**, 3967–3969. (doi:10.1063/1.1150021)
35. Song Y, Wu S, Xu L, Fu X. 2015 Accurate calibration and uncertainty estimation of the normal spring constant of various AFM cantilevers. *Sensors* **15**, 5865–5883. (doi:10.3390/s150305865)
36. Kalpakjian S, Schmid S. 2014 *Manufacturing processes for engineering materials*, 5th edn. Upper Saddle River, NJ: Pearson Prentice Hall.
37. Ulusoy E, Kolayli S. 2014 Phenolic composition and antioxidant properties of Anzer bee pollen. *J. Food Biochem.* **38**, 73–82. (doi:10.1111/jfbc.12027)
38. Bal S, Behera R. 2006 Structural investigation of chemical treated polyester fibers using SAXS and other techniques. *J. Miner. Mater. Characterization Eng.* **5**, 179–198. (doi:10.4236/jmmce.2006.52013)
39. Lin H, Lizarraga L, Bottomley LA, Carson Meredith J. 2015 Effect of water absorption on pollen adhesion. *J. Colloid Interface Sci.* **442**, 133–139. (doi:10.1016/j.jcis.2014.11.065)
40. Weeks BL, Vaughn MW, DeYoreo JJ. 2005 Direct imaging of meniscus formation in atomic force microscopy using environmental scanning electron microscopy. *Langmuir* **21**, 8096–8098. (doi:10.1021/la0512087)
41. Wang Y, Len T, Huang Y, Diego Taboada A, Boa AN, Ceballos C, Delbecq F, Mackenzie G, Len C. 2017 Sulfonated sporopollenin as an efficient and recyclable heterogeneous catalyst for dehydration of D-xylose and xylan into furfural. *ACS Sustain. Chem. Eng.* **5**, 392–398. (doi:10.1021/acssuschemeng.6b01780)
42. Cousins W. 1976 Elastic modulus of lignin as related to moisture content. *Wood Sci. Technol.* **10**, 9–17. (doi:10.1007/BF00376380)
43. Kojima H, Ishijima A, Yanagida T. 1994 Direct measurement of stiffness of single actin filaments with and without tropomyosin by *in vitro* nanomanipulation. *Proc. Natl Acad. Sci. USA* **91**, 12 962–12 966. (doi:10.1073/pnas.91.26.12962)
44. Gittes F, Mickey B, Nettleton J, Howard J. 1993 Flexural rigidity of microtubules and actin filaments measured from thermal fluctuations in shape. *J. Cell Biol.* **120**, 923–934. (doi:10.1083/jcb.120.4.923)
45. Höije A, Gröndahl M, Tømmeraas K, Gatenholm P. 2005 Isolation and characterization of physicochemical and material properties of arabinoxylans from barley husks. *Carbohydr. Polym.* **61**, 266–275. (doi:10.1016/j.carbpol.2005.02.009)
46. Zhang P, Whistler RL. 2004 Mechanical properties and water vapor permeability of thin film from corn hull arabinoxylan. *J. Appl. Polym. Sci.* **93**, 2896–2902. (doi:10.1002/app.20910)
47. Skendi A, Biliaderis C, Lazaridou A, Izydorczyk M. 2003 Structure and rheological properties of water soluble β-glucans from oat cultivars of *Avena sativa* and *Avena bysantina*. *J. Cereal Sci.* **38**, 15–31. (doi:10.1016/S0733-5210(02)00137-6)
48. van der Rijt JA, van der Werf KO, Bennink ML, Dijkstra PJ, Feijen J. 2006 Micromechanical testing of individual collagen fibrils. *Macromol. Biosci.* **6**, 697–702. (doi:10.1002/mabi.200600063)
49. Buehler MJ. 2007 Nano-and micromechanical properties of hierarchical biological materials and tissues. *J. Mater. Sci.* **42**, 8765–8770. (doi:10.1007/s10853-007-1952-8)